A Sequential Monte Carlo Framework for Noise Filtering in InSAR Time Series

Mehdi Khaki, Mick S. Filmer, Will E. Featherstone, Michael Kuhn, Luyen K. Bui, and Amy L. Parker

***Abstract*— This article proposes an alternative filtering technique to improve interferometric synthetic aperture radar (InSAR) time series by reducing residual noise while retaining the ground deformation signal. To this end, for the first time, a data-driven approach is introduced, which is based on Takens's method within the sequential Monte Carlo framework, allowing for a model-free approach to filter noisy data. Both a Kalman-based filter and a particle filter (PF) are applied within this framework to investigate their impact on retrieving the signals. More specifically, PF and particle smoother [PaSm; to avoid confusion with persistent scatterers (PSs)] are tested for their ability to deal with non-Gaussian noise. A synthetic test based on simulated InSAR time series, as well as a real test, is designed to investigate the capability of the proposed approach compared with the spatiotemporal filtering of InSAR time series. Results indicate that PFs and more specifically PaSm perform better than other applied methods, as indicated by reduced errors in both tests. Two other variants of PF and adaptive unscented Kalman filter (AUKF) are presented and are found to be able to perform similar to PaSm but with reduced computation time. This article suggests that PFs tested here could be applied in InSAR processing chains.**

***Index Terms*— Data-driven technique, interferometric synthetic aperture radar (InSAR), non-Gaussian noise, particle filter (PF), sequential technique.**

I. Introduction

MONITORING deformation (primarily subsidence/uplift) of the Earth's surface is important to understand its physical processes and the resulting hazards, e.g., earthquake, volcanoes, landslides, anthropogenic subsidence, or uplift. Various techniques are employed to do this, but interferometric synthetic aperture radar (InSAR) has become a standard tool to undertake such studies by remotely sensing large areas at high spatial and temporal resolutions [1]. In principle, InSAR uses two complex SAR images from repeat satellite passes to produce an interferogram over the common area. For a review of InSAR fundamentals, see [2].

Individual interferograms are highly sensitive to various noise sources, such as those attributed to spatial and temporal decorrelations [3], atmospheric effects [2], topographic effects, thermal noise, and orbit errors [4]. These can affect the sought-after deformation signal, both in the estimated velocities and the time series. Advances in processing methods, such as multitemporal InSAR where multiple interferograms are "stacked" [5], persistent scatterers (PSs) [6], small baseline subset (SBAS) [7], and a combination of these approaches [8] can help reduce the effects of noise on the computed velocity, especially when a long time series with a large number of SAR scenes is available.

For deformation time series of interest to investigate geophysical events, the noise in the estimated displacement may be more problematic. The major source of noise in the InSAR time series is the combination of tropospheric delay, which comprises vertical stratification and turbulent components [2]. The vertical stratification component can be estimated by its relation with height [9], but the turbulent component is variable in flat areas, so more difficult to determine [10].

Various filtering methods are used at different stages of InSAR processing. For example, the Goldstein filter [11] is applied to the wrapped interferogram phase to reduce noise and improve the unwrapping process. A filter parameter (α) is implemented that can be set between zero and one; if set to zero, no filtering is done, while a setting of one will result in heavy filtering that is likely to significantly change the structure of the interferogram [12]. Reference [8] uses a spectral filter on small baseline interferograms to assist in the selection of slowly decorrelating filtered phase (SDFP) pixels used in his combined SBAS and PS method. Spatiotemporal filtering (STF) is used in [13] in the Stanford method for PSs (StaMPS) (see also [14]) on postprocessed PS to reduce temporal noise in the time series (mostly time- and space-variable turbulent tropospheric noise [10]) and for spatial noise relative to other PSs. Like all filters, this can be set at different temporal and spatial scales, which will tend to remove noise, but may also remove parts of the sought-after deformation signal, particularly where the noise and deformation display similar characteristics in time and/or space [15].

Here, we focus on reducing residual noise with a view to reducing processing and observation noise in the InSAR time series. A number of methods have been used to estimate this component [10], [16]. The difficulty with applying such filters is that they can remove most noise present but at the cost of the geophysical signal of interest. Hence, it is a balance to "tune" the filter so that its spatial and temporal settings can be "optimal" to remove as much noise as possible while retaining

Manuscript received July 21, 2019; revised October 3, 2019; accepted October 21, 2019. Date of publication November 26, 2019; date of current version February 26, 2020. *(Corresponding author: Mehdi Khaki.)*

M. Khaki is with the School of Engineering, University of Newcastle, Callaghan, NSW 2308, Australia (e-mail: mehdi.khaki@newcastle.edu.au).

M. S. Filmer, W. E. Featherstone, M. Kuhn, L. K. Bui, and A. L. Parker are with the School of Earth and Planetary Sciences, Spatial Sciences, Curtin University, Perth, WA 6845, Australia.

Color versions of one or more of the figures in this article are available online at http://ieeexplore.ieee.org.

Digital Object Identifier 10.1109/TGRS.2019.2950353

the information of interest. Notably, the STF employed in StaMPS assumes Gaussian noise, yet geophysical signals of interest may be nonlinear in time, e.g., aseismic slip, or slow-moving landslides [14].

The main objective of this article is, therefore, to test some alternative filters that may improve upon results from STF (e.g., available in StaMPS) to reduce the noise in InSAR time series. Different studies have been undertaken to improve the signal-to-noise ratio in InSAR signals, especially prior to the unwrapping process [11], [17]. These filters can generally be categorized into two groups, i.e., filtering in the spatial [19], [20] and frequency [11], [21] domains. These filters have been shown to be effective for smoothing as well as dealing with nonlinear phase noises [22]. Nevertheless, there are a number of factors that degrade the performance of spatial and spectral filters. For example, multiple interferograms are required in most of these filters to better model noise, especially atmospheric noise [23]. The methods also rely excessively on coherent pixel-wised data, which may not always be available [24]. The spatiotemporal filters, despite being easier to apply due to their simplicity, can alter or remove the fringe structures in the signals [22]. A number of studies have been put forward to address this [25], [26]. Furthermore, the Gaussian noise assumption is a fundamental principle in a large group of filters, which, in reality, may not always be the case [27].

In order to address these problems, an alternative InSAR filtering approach is proposed here. The technique is based on a data-driven method, namely Takens's filter [28]–[30]. Our proposed approach implements the Takens method for attractor reconstruction within the sequential Monte Carlo framework, allowing for a model-free approach to filter noisy data [31]. Based on Takens's theorem, equations underlying a model, which describe the time evolution of a system, e.g., land deformation time series, can be replaced by the information contained in the data. This, along with the implementation of Monte Carlo techniques, such as Kalman filters (KFs) and particle filters (PFs) for updating the system based on the current data, allows the handling of noise in the observed data [29].

Here, for the first time, we apply the Takens filter to reduce residual noise in InSAR data. Contrary to previous studies that used KF and PF techniques for phase unwrapping and/or noise reduction [32], [33], the Takens method relies only on data and avoids assumptions on the state-space model noises and can be computationally faster [30]. To assess the performance of the Takens method, we tested it on synthetic and real data and compared with [13] STF, which is usually applied to postprocessed PS.

II. Methodology

The proposed filtering scheme comprises two steps in a sequential process, i.e., forecast then analysis, similar to data assimilation techniques [34]–[36]. Sequential methods do not require an adjoint (like variational methods) and are becoming increasingly popular because of their reasonable computational requirements, as they do not need to record and use historical data. In the forecast step, the state estimate at time t (e.g., land deformation) and its corresponding probability density function (PDF) are forwarded in time to $t+1$ using a state transition operator. Monte Carlo methods are commonly used in the forecast step (based on ensembles or particles). These are then filtered in the analysis step based on the likelihood of the observations (e.g., simulated observations). Traditionally, a dynamical model is used in the forecast step; however, a problem arises when a model is not available. To address this, the Takens filter is applied to form the state transition operator (see Section II-A). Various filtering methods can then be used for the analysis step to update forecast PDF such as Kalman (e.g., ensemble Kalman filtering) or point-mass weight (e.g., PF). Here, three variants of most commonly used sequential techniques, i.e., adaptive unscented Kalman filter (AUKF), PF, and particle smoother (PaSm), are applied (see Sections II-B–II-C). We also test STF [13] to assess the capability of the proposed filtering method. The STF is "tuned" to determine the "optimal" settings for the comparison. This includes applying different values for various parameters used in the STF, such as bandpass phase filters and low-pass cutoff, to reach the best performance compared to the "truth." The corresponding outcomes are then used to evaluate the proposed filtering scheme.

A. Takens's Filter

The Takens filter does not rely on a model and its corresponding equations, which significantly decreases the computational burden with comparable outcomes with respect to a standard case. The absence of a model in the InSAR time series filtering process makes the Takens filter a potential candidate to be used for forecasting. Reference [29] showed that this filter has a high capability for time series filtering in the presence of various noises. The Takens method is used to reconstruct the model, e.g., following the terminology of [30] shown by $\mathbf{f}$, for the forecast step with a local proxy $\tilde{\mathbf{f}}$. This is done using a set of training data based on the InSAR time series to represent the state of the system. The training data are obtained from the delay vector as well as neighboring grid points. The delay vector $\mathbf{x}$ (at t) can be formed using the historical state variables, e.g., d temporal delays of InSAR line of sight (LoS), $\mathbf{x}^{\circ}$, following:

$$\mathbf{x}_t = [\mathbf{x}^{\circ}{}_t, \mathbf{x}^{\circ}{}_{t-1}, \ldots, \mathbf{x}^{\circ}{}_{t-d}]. \tag{1}$$

Next, similar delay vectors located at the N nearest neighbors, i.e., grid points located close to the point of interest (based on Euclidean distance) within a set of training data, are derived by

$$\begin{aligned} \mathbf{x}_t^1 &= \left[\mathbf{x}^{\circ 1}{}_t, \mathbf{x}^{\circ 1}{}_{t-1}, \ldots, \mathbf{x}^{\circ 1}{}_{t-d}\right] \\ \mathbf{x}_t^2 &= \left[\mathbf{x}^{\circ 2}{}_t, \mathbf{x}^{\circ 2}{}_{t-1}, \ldots, \mathbf{x}^{\circ 2}{}_{t-d}\right] \\ &\vdots \\ \mathbf{x}_t^N &= \left[\mathbf{x}^{\circ N}{}_t, \mathbf{x}^{\circ N}{}_{t-1}, \ldots, \mathbf{x}^{\circ N}{}_{t-d}\right]. \end{aligned} \tag{2}$$

Once delay vectors are calculated, a local model can be created for the forecast step, i.e., to advance state from t to $t+1$ and correspondingly $\mathbf{x}_t$ to $\mathbf{x}_{t+1}$. The local model $\tilde{\mathbf{f}}$ can then be generated (in its simplest from) using a weighted average of the training data according to

$$\mathbf{x}_{t+1} = \omega_1 \gamma^{\,1} \mathbf{x}_{t+1}^1 + \omega_2 \gamma^{\,2} \mathbf{x}_{t+1}^2 + \cdots + \omega_N \gamma^{\,N} \mathbf{x}_{t+1}^N \tag{3}$$

with

$$\omega_i = \frac{e^{-(d_i/\sigma)^2}}{\sum_{j=1}^{N} e^{-(d_j/\sigma)^2}} \tag{4}$$

where the distance between the jth neighbor of $\mathbf{x}_t$ is indicated by d_i. σ is applied to control the contribution of each neighbor in the local model and it is called a bandwidth parameter (here $\sigma = 2$). γ^k, $k = 1, \ldots, N$ in (3) refers to the coherence factor, which is calculated as an absolute value of the correlation coefficient between two SAR scenes following:

$$\gamma_{1,2} = \frac{||E(z_1, z^*_2)||}{\sqrt{E(||z_1||^2) \cdot E(||z_2||^2)}} \tag{5}$$

where z_1 and z_2 are the complex returns for two SARs and $E(.)$ represents the expectation function. The inclusion of coherence in the local model formulation decreases the effect of noisy observations with smaller γ. Afterward, the forecast state $\mathbf{x}_{t+1}$ is updated in the next step based on Bayes's rule [34]. This is done to update the forecast state based on the current observations.

As shown in [29], the availability of unpredictable noise components in the observed data is a common context for the application of the Kalman–Takens filter, which is able to handle observation noise using sequential forecast and update steps. Applying this method to the entire training data set reduces the observation noise in the training data, which will improve future filtering and also provide better neighbors to improve forecasting [37]. The application of the Kalman–Takens filter also allows for better quantification of the uncertainty in the state, e.g., through the state forecast covariance matrix, which will then be reduced using the update step (see Sections II-B–II-C). While delay coordinate embedding replaces the missing model, the Kalman (or particle) update offers a maximum likelihood estimate of the reconstructed state in the presence of noise. This combination of two filters, therefore, contains complementary strengths of the two.

Three different methods from the sequential Monte Carlo framework are used for the update step. These include AUKF [38], PF [39], and PaSm [40]. The Kalman-based and PFs are specifically selected due to their ability to deal with different types of noise. When non-Gaussian noise exists, the particle approach is particularly well suited [39]. These filters are based on point mass representations of probability densities, which generalize the traditional KF and do not rely on a Gaussian noise assumption.

B. AUKF

An AUKF is based on the Monte Carlo scheme, which generates random variables and propagates them through a nonlinear function using a deterministic sampling approach for producing $2L + 1$ sigma points with L being the dimension of the state as

$$\mathbf{x}_t^0 = \mathbf{x}_t \tag{6}$$

$$\mathbf{x}_t^i = \mathbf{x}_t + (\sqrt{(L+\lambda)\mathbf{P}_t})_i \quad i = 1, \ldots, L \tag{7}$$

$$\mathbf{x}_t^{i+L} = \mathbf{x}_t - (\sqrt{(L+\lambda)\mathbf{P}_t})_i \quad i = 1, \ldots, L \tag{8}$$

where $\mathbf{P}_t$ represents the state covariance matrix. The associated weights to the sigma points are estimated by

$$w_s^0 = \frac{\lambda}{(L+\lambda)} \tag{9}$$

$$w_c^0 = \frac{\lambda}{(L+\lambda)} + (1 - \alpha^2 + \beta) \tag{10}$$

$$w_s^i = \frac{1}{2(L+\lambda)} \quad i = 1, \ldots, 2L \tag{11}$$

where λ is the scaling parameter with $\lambda = \alpha^2(L + \beta) - L$. α (0–1) controls the spread of the sigma points and β is usually set to 0 [41]. The generated sigma points are then integrated with a model using the local proxy $\tilde{\mathbf{f}}$ created in the Kalman–Takens filter to estimate the forecast state. Once done, the forecast averages and corresponding covariance matrices are calculated following [41]:

$$\mathbf{x}_{t+1}^f = \sum_{j=0}^{2L} \mathbf{w}_s^j \mathbf{x}_{t+1}^{f,j} \tag{12}$$

$$\mathbf{y}_{t+1}^f = \sum_{j=0}^{2L} \mathbf{w}_s^j \mathbf{H}\mathbf{x}_{t+1}^{f,j} \tag{13}$$

where $\mathbf{H}$ is the observation operator that maps the model states into the observation space to update state estimates. Next, the analysis step is employed, which updates the forecast state $\mathbf{x}_{t+1}^f$ using incoming observations $\mathbf{y}_{t+1}$ to calculate the analysis state $\mathbf{x}_{t+1}^a$ based on the Kalman update equations

$$\mathbf{x}_{t+1}^a = \mathbf{x}_{t+1}^f + \mathbf{K}(\mathbf{y}_{t+1} - \mathbf{y}_{t+1}^f) \tag{14}$$

with $\mathbf{K}$ being the Kaman gain and calculated according to covariance matrices associated with the process ($\mathbf{Q}_t$) and observation ($\mathbf{R}_{t+1}$) (see more details in [41]). Critical to the success of this method is the selection of the filter noise covariance and, in particular, the process noise covariance matrix $\mathbf{Q}$. Reference [38] shows that unscented KF performance is highly dependent on $\mathbf{Q}$, especially for nonlinear problems. Here, we use the method of [38] to adaptively estimate this covariance matrix. The general idea of [38] is to use the increment, $\epsilon_t = \mathbf{y}_t - \mathbf{y}_t^f$, to estimate the noise covariance at each time step, as per [38].

C. PF

PF is also a sequential Monte Carlo method, which represents the state PDF by a set of weighted particles [39]. The state PDF is then decomposed as

$$P(\mathbf{x}_t|\mathbf{y}_{1:t}) \approx \sum_{i=1}^{M} \omega_t^i \delta\left(\mathbf{x}_t - \mathbf{x}_t^i\right) \tag{15}$$

where $\{\mathbf{x}_t^i; i = 1 \ldots M\}$ (with M being the particle size) are the particles at time t, observations between time 1 and t are denoted by $\mathbf{y}_{1:t}$, ω_t^i are the weights of the particles (normalized importance weight), and δ is the Dirac delta function. In the forecast step, PF just integrates the particles forward with the local proxy $\tilde{\mathbf{f}}$, exactly as AUKF, and their weights remain

the same. In the analysis step, only the weights, and not the particles, are updated using

$$\omega_t^i = \frac{P\left(\mathbf{y}_t|\mathbf{x}_{t|t-1}^i\right)}{\sum_j P\left(\mathbf{y}_t|\mathbf{x}_{t|t-1}^j\right)}. \tag{16}$$

PaSm is also applied in a largely similar manner by propagating particle members and their associated weights in the forecast step and updating the latter in the analysis step. The main difference between the two approaches is estimation of the state distribution. Contrary to PF, the distribution at a particular time is calculated in PaSm using all the observations up to some later time. This results in using additional information (e.g., taking advantage of a few later observations), which leads to smoother estimates than PF and likely to a better performance, especially if state estimation at a particular time is not required instantly [40]. A forward–backward smoother is assumed here, which proceeds by first making a forward filtering pass to compute the filtered distribution at each time step, and then a backward smoothing pass to determine the smoothing distribution [42]. The distribution can be approximated by

$$P(\mathbf{x}_t|\mathbf{y}_{1:T}) \approx \sum_{i=1}^{M} \omega_{t|T}^i \delta\left(\mathbf{x}_t - \mathbf{x}_t^i\right) \tag{17}$$

with $\mathbf{y}_{1:T} = \{\mathbf{y}_1 \ldots \mathbf{y}_T\}$, $(T \geq t+1)$ and corresponding particle weights of

$$\omega_{t|T}^i = \omega_t^i \left[\sum_{j=1}^{M} \omega_{t+1|T}^j \frac{P\left(\mathbf{x}_{t+1}^j|\mathbf{x}_t^i\right)}{\sum_{k=1}^{N} \omega_t^k P\left(\mathbf{x}_{t+1}^j|\mathbf{x}_t^k\right)}\right]. \tag{18}$$

A resampling technique of systematic resampling [43] is applied to account for the so-called "degeneracy problem" in which the weights of all particles become negligible except only for a very few, requiring a prohibitive number of particles to prevent the particles collapsing [39]. The method draws only one random number $u_1 \sim U(0, 1/N)$ and the remaining $N-1$ numbers are then calculated from u_1 as

$$U_i = u_1 + \frac{(i-1)}{M}, \quad i = 2 \ldots M. \tag{19}$$

These are then used to select a new set of particles according to the multinomial distribution [39]. Fig. 1 shows a summary of the filtering framework and the applied filters for the InSAR noise reduction process in this article.

III. Experiment Setups

A. Synthetic Data

InSAR LoS phase observations and their associated errors are simulated following [18] and [23] with similar average properties to the TerraSar-X satellite mission [44]. The simulation is done over the Perth (WA, Australia) metropolitan region with 11-day repeats from October 2012 to October 2016 within the spatial extents of $32.25°S$–$31.65°S$ and $115.60°E$–$116.10°E$ with ~30 m pixel size. In summary, the process includes introducing land subsidence using the point pressure model, simulating topographic errors, atmospheric artifacts, orbital errors, and temporal decorrelations as per [18], and lastly creating interferograms. We then apply the 3-D phase unwrapping method in StaMPS small baseline MTI [14]. Once the synthetic interferograms are produced, they are merged and converted to deformation time series. To this end, small baseline subset (SBAS) is used with the spatial perpendicular baselines less than 150 m and temporal baselines less than 100 days. The proposed filtering methods are then applied to the simulated LoS data. These synthetic data are simpler than real interferograms and do not include, e.g., nonlinear phase-topography gradients and quadratic orbital ramps. Nevertheless, they can sufficiently reproduce the primary features of InSAR data for testing the proposed filters. For an additional analysis, real data will be considered in Section III-B.

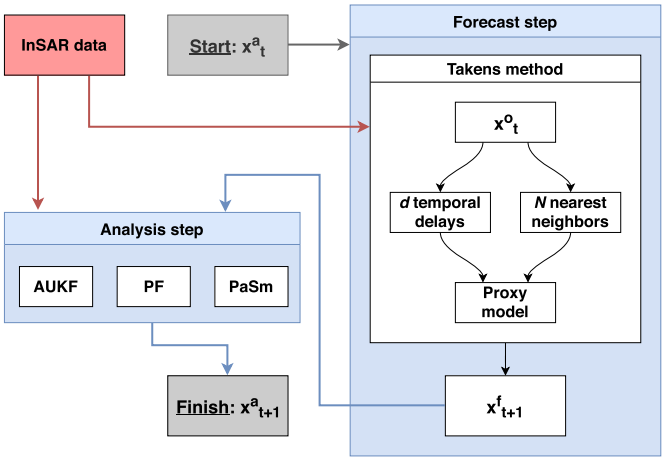

Fig. 1. Schematic of the filtering steps based on the Takens method, as well as sequential techniques, i.e., AUKF, PF, and PaSm at every assimilation cycle.

B. Real Data

The InSAR component of the real test data used 109 X-band scenes (wavelength 3.1 cm) over Perth, WA, Australia, from the TerraSAR-X (TSX) satellite mission under the German Aerospace Center (DLR) science project LAN1499. The scenes were acquired between October 2012 and October 2016 with a temporal resolution of 11 days but with some gaps due to operational priorities for the satellite. The 109 scenes were used to process 442 SBAS interferograms using the Doris software [45] within StaMPS small baseline MTI processing [14]. The SDFP pixels [8] were downsampled to 30-m spatial resolution using the procedure described in [14] to reduce the many millions of SDFP pixels to a manageable data set. Long-wavelength orbit and ionospheric effects were accounted for via the estimation and removal of a phase ramp, which is suitable for the TSX scene extent of 30×50 km [14]. The LoS deformation time series was computed from the SBAS interferogram SDFP differences.

The time series is filtered to reduce the residual noise using various filters, including the proposed Takens approach. The results are then compared with GPS time series over the study period (October 2012 to October 2016), which is provided by the Nevada Geodetic Laboratory (http://geodesy.unr.edu/)

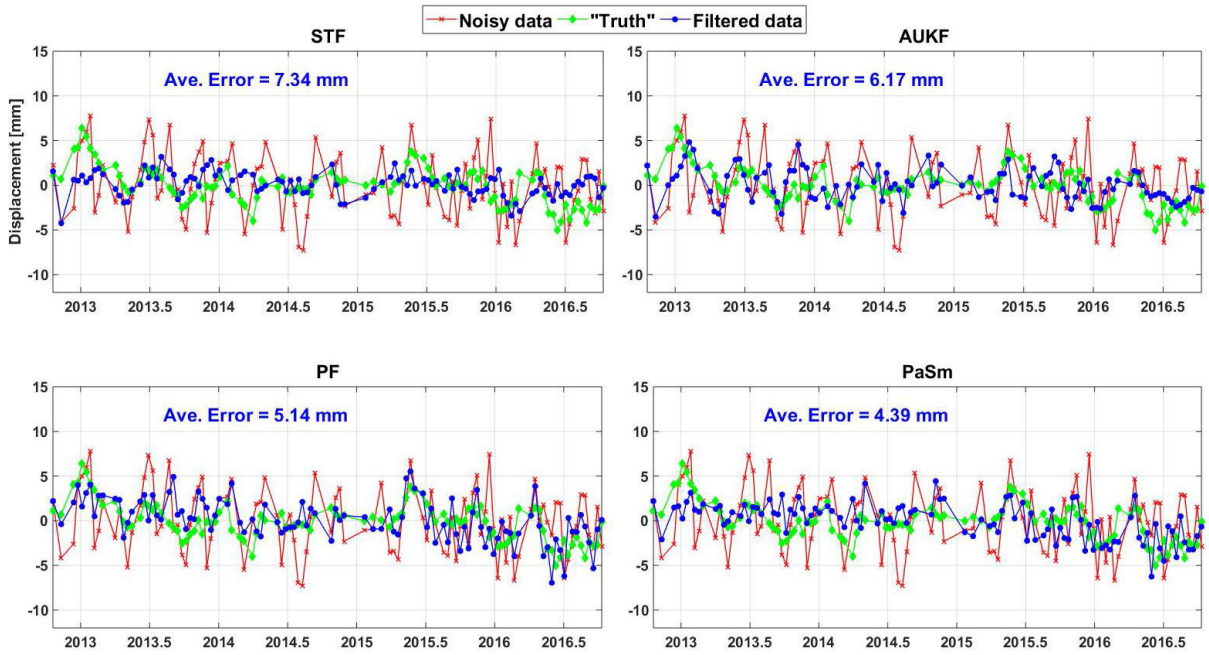

Fig. 2. InSAR time series at a randomly selected point (latitude −31.802° and longitude 115.885°) from different filtering scenarios based on the synthetic data compared to the no filter results and the "truth." Note that average errors between the filtered times series and "truth" are indicated on each subfigure. The average error of noisy (unfiltered) data is 10.29 mm.

for the international GNSS service (IGS) station "PERT" in Perth. GPS data are used to assess the performance of the InSAR filters in the real test, albeit for a single site and not whole area.

IV. Results and Discussion

A. Synthetic Test

An evaluation of the proposed filters, also compared to the existing method of STF, is assumed in this section. The main objective is to reduce the impact of noise by applying different filters and retrieve the artificially introduced subsidence signals from the simulated phase. To this end, all the filters are applied to the synthetic data using their "optimum" configurations and their results are validated against the unperturbed data (the simulated "truth"). Fig. 2 shows the time series (at a single location) from the perturbed (red) and unperturbed (green) LoS deformation, as well as the results of each filter applied (blue). Moreover, detailed results can be found in Table I, where maximum differences, RMSE, standard deviation (STD), and correlation coefficients are reported. In Table I, average results over the entire scene are presented. Fig. 2 shows that the application of all the filters decreases the misfits with respect to the unperturbed displacements. The level of improvement, however, is different for different filters, as it can also be seen from the indicated average error for each case. These errors are calculated as the average of absolute differences between the filtered time series and the unperturbed time series. The PFs, and particularly PaSm, achieve the "best" results. We gauge "best" as the closest agreement with the simulated "truth" as determined by the lowest RMSE and highest correlation coefficient (see Table I). PaSm reduces RMSE from 10.30 mm in the perturbed data to 6.63 mm (a reduction of 36%).

The weakest performance belongs to the STF based on both Fig. 2 and Table I. The correlation between filtered and unperturbed ("truth") time series for the STF is 0.57, smaller than PF (0.78) and PaSm (0.89). From Fig. 2, in general, smoother time series is obtained from the AUKF, which is observed to better alleviate high-frequency noise than STF and PF. This resulted in smaller STD (6.17 mm) compared to STF (7.34 mm) and PF (6.81 mm). PaSm is found to better improve the time series, which contrary to other filters, do not rely on a Gaussian noise assumption. This allows the particle approaches to model the errors more realistically, leading to better performance especially for PaSm, e.g., with the lowest RMSE (4.22 mm) and the highest correlation (0.89). The most promising results among the three proposed filter variants also belong to PaSm, slightly better than PF, which can be attributed to the applied forward–backward algorithm allowing for using more information in the filtering process.

Spatial distributions of the displacement errors (i.e., the misfit between the results and the simulated "truth") based on the simulated data are shown in Fig. 3. At each grid point, the temporally averaged error (i.e., average of error time series at each grid point) is calculated for all these filters, as well as when no filter (noisy data) is applied. Smaller errors are found from PF and PS, and to a lesser degree AUKF, than STF. These can be inferred from the lower differences over the entire area, which supports the previous results indicating the superiority of the proposed methods. Another major discrepancy among the STF errors maps with those of the new filters refers to a smoother spatial pattern in the latter (see Fig. 3). The smoother errors maps of PF, PaSm, and AUKF can be explained by the use of neighboring points in reconstructing the model for the Takens approach. The proxy model is constructed from N neighbor points, which means implicit spatial smoothing

TABLE I

SUMMARY OF STATISTICS DERIVED FROM IMPLEMENTING DIFFERENT FILTERS (WITH RESPECT TO "TRUTH") ON THE SIMULATED INSAR TIME SERIES (2012–2016 FOR ALL FILTERS) AND OVER THE WHOLE AREA. RMSE REDUCTION IS WITH RESPECT TO ORIGINAL DATA (I.E., NO FILTER APPLIED)

Filter	Max error (mm)	RMSE (mm)	STD (mm)	Correlation	RMSE reduction (%)
No filter	13.35	10.30	9.72	0.38	–
STF	12.08	8.56	7.34	0.57	17
AUKF	9.78	7.46	6.81	0.66	28
PF	9.35	7.11	6.17	0.78	31
PaSm	7.49	6.63	4.22	0.89	36

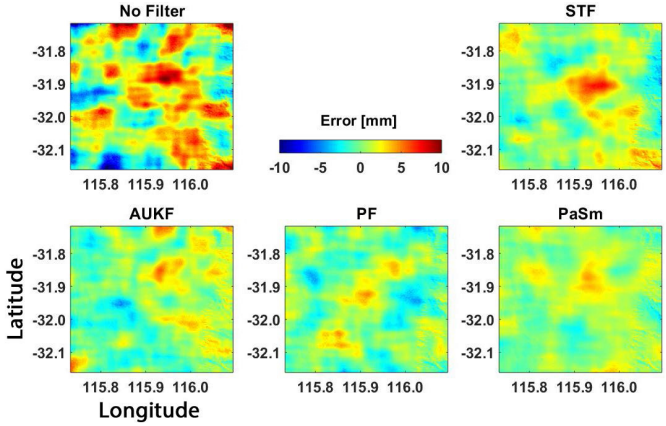

Fig. 3. Temporally averaged "error" maps from different filtering scenarios (mm). Error is the difference between the filtered results and "truth" data.

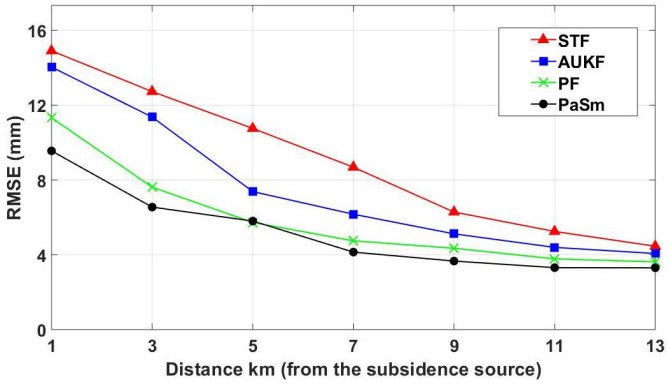

Fig. 4. Filters' average RMSE results at constant distances from the simulated deformation source.

is applied in the filter's forecast steps. Fig. 3 also shows that the PaSm results in a smoother spatial pattern and smoother error time series than PF due to the former implementing the filtering followed by a smoothing process [46], while the latter only applies filtering.

Larger errors can be found around the imposed deformation source. Such larger error amplitudes are more pronounced in the STF and AUKF "error" maps, yet, much lesser than the error map of noisy data. To better represent this, the filters' RMSE results at constant distances from the deformation source are compared in Fig. 4. For this purpose, RMSE values are spatially interpolated to these radial distances using the nearest neighbor approach. As the distance increases, the error values for all filters decrease but this is more noticeable for STF, which demonstrates the largest error close to the deformation source. Again, PaSm and, to a lesser degree, PF hold the best performance slightly better than AUKF and considerably better than STF. Overall, similar to the previous results, the particle approaches (PF and PaSm) obtain "better" results against the other applied filters.

B. Real Test

To further investigate the performance of the filters in a more realistic scenario, their results from real InSAR data from TerraSar-X are compared with GPS time series. This is not an optimal evaluation, as GPS data are subject to various error sources, which can be different than those in InSAR data. However, in the absence of reliable validation data, such an evaluation may provide some insight into which the filtering method can better reflect the land displacements albeit at one point. Fig. 5 shows the time series of InSAR data (red), GPS (green), and filtered time series (blue). The comparison is done over a GPS station between InSAR data filtered by various methods and GPS time series (see Fig. 5), which is converted to LoS data based on the TerraSar-X satellite look and heading angles (following [47, eq. (1)]). The correlation values, i.e., between each two time series are also indicated for each case. Improvements can be seen for all the applied filters based on the better agreement between the filtered results and GPS data. Nevertheless, better results are provided by PFs. In some time periods, e.g., after 2015, large misfits between the STF results and GPS observations exist. AUKF, PF, and PaSm, on the other hand, provide better results (smaller differences to GPS), which shows their ability to better capture changes. However, larger correlation values are obtained between PF and PaSm results and GPS data. Overall, AUKF, PF, and PaSm time series indicate better agreement with the GPS data. The best performance is obtained from applying PaSm with 0.74 correlation to GPS time series against 0.34 for STF, 0.53 for AUKF, and 0.69 for

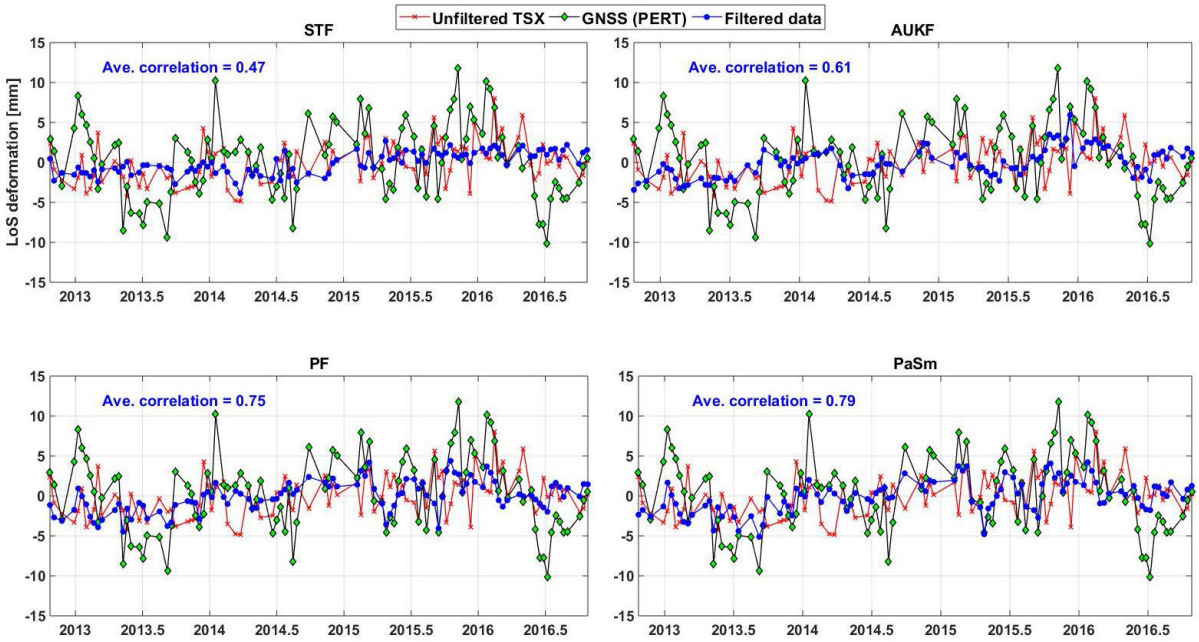

Fig. 5. InSAR time series at "PERT" station (latitude −31.802° and longitude 115.885°) from different filtering scenarios using TerraSar-X data compared to no filter and the GPS time series. Note that the correlation between the filtered times series and GPS is indicated on each subfigure. The correlation between noisy data and GPS time series is 0.18.

PF. These results agree with the synthetic experiment results, in which PFs also performed better.

V. Conclusion

An alternative InSAR noise filtering scheme was proposed in this article, which comprises different steps, including the Takens method for attractor reconstruction, followed by the sequential Monte Carlo framework, allowing for a model-free approach to filter noisy data. The method has significant benefits because of its capability to deal with non-Gaussian noise. A synthetic test was designed based on the simulated InSAR LoS phase data to investigate the capability of the proposed approach compared with the STF with the results indicating that the particle approaches (PF and PaSm), and to a lesser degree AUKF, show a larger reduction in residual noise both temporally and spatially. Specifically, PaSm successfully reduced RMSE by 34%, approximately 5%, 10%, and 15% better than PF, AUKF, and STF, respectively. Moreover, PFs, especially PaSm, appear to agree better with GPS in a real test. The capability of PaSm and PF in dealing with non-Gaussian noise can explain their better performance, especially against the Kalman-based filter AUKF; however, for the PaSm, this was obtained at the expense of a heavier computational burden. PF, on the other hand, achieved the closest performance among other filters in a more efficient manner, e.g., in terms of processing time and complexity. The next alternative can be AUKF, which is highly capable of reducing noise using much less population size. These results suggest that the PFs tested here using the Takens approach can offer alternative methods for dealing with noisy InSAR signals, which depends on the filters' optimization.

Acknowledgment

The authors would like to thank the German Aerospace Center (DLR) science project LAN1499 for providing TSX data, and the Nevada Geodetic Lab for providing GPS data. They would also like to thank A. Hooper for StaMPS software. Further material useful for readers to understand and reproduce synthetic data sets, as well as additional results evaluation can be obtained by contacting the corresponding author.

References

[1] D. Massonnet and T. Rabaute, "Radar interferometry: Limits and potential," *IEEE Trans. Geosci. Remote Sens.*, vol. 31, no. 2, pp. 455–464, Mar. 1993.

[2] R. F. Hanssen, *Radar Interferometry: Data Interpretation and Error Analysis*. New York, NY, USA: Springer, 2001, p. 308.

[3] H. A. Zebker and J. Villasenor, "Decorrelation in interferometric radar echoes," *IEEE Trans. Geosci. Remote Sens.*, vol. 30, no. 5, pp. 950–959, Sep. 1992, doi: 10.1109/36.175330.

[4] H. Bähr and R. F. Hanssen, "Reliable estimation of orbit errors in spaceborne SAR interferometry," *J. Geodesy*, vol. 86, no. 12, pp. 1147–1164, 2012, doi: 10.1007/s00190-012-0571-6.

[5] D. T. Sandwell and E. J. Price, "Phase gradient approach to stacking interferograms," *J. Geophys. Res.*, vol. 103, no. B12, pp. 30183–30204, Dec. 1998, doi: 10.1029/1998JB900008.

[6] A. Ferretti, C. Prati, and F. Rocca, "Permanent scatterers in SAR interferometry," *IEEE Trans. Geosci. Remote Sens.*, vol. 39, no. 1, pp. 8–20, Jan. 2001.

[7] P. Berardino, G. Fornaro, R. Lanari, and E. Sansosti, "A new algorithm for surface deformation monitoring based on small baseline differential SAR interferograms," *IEEE Trans. Geosci. Remote Sens.*, vol. 40, no. 11, pp. 2375–2383, Nov. 2002.

[8] A. Hooper, "A multi-temporal InSAR method incorporating both persistent scatterer and small baseline approaches," *Geophys. Res. Lett.*, vol. 35, no. 16, 2008, Art. no. L16302, doi: 10.1029/2008GL034654.

[9] D. P. S. Bekaert, A. Hooper, and T. J. Wright, "Reassessing the 2006 Guerrero slow-slip event, Mexico: Implications for large earthquakes in the Guerrero Gap," *J. Geophys. Res.*, vol. 120, no. 2, pp. 1357–1375, 2015, doi: 10.1002/2014JB011557.

[10] Y. Cao, Z. Li, J. Wei, J. Hu, M. Duan, and G. Feng, "Stochastic modeling for time series InSAR: With emphasis on atmospheric effects," *J. Geodesy*, vol. 92, no. 2, pp. 185–204, 2018, doi: 10.1007/s00190-017-1055-5.
[11] R. M. Goldstein and C. L. Werner, "Radar interferogram filtering for geophysical applications," *Geophys. Res. Lett.*, vol. 25, no. 21, pp. 4035–4038, Nov. 1998, doi: 10.1029/1998GL900033.
[12] I. Baran, M. P. Stewart, B. M. Kampes, Z. Perski, and P. Lilly, "A modification to the Goldstein radar interferogram filter," *IEEE Trans. Geosci. Remote Sens.*, vol. 41, no. 9, pp. 2114–2118, Sep. 2003.
[13] A. Hooper, P. Segall, and H. Zebker, "Persistent scatterer interferometric synthetic aperture radar for crustal deformation analysis, with application to Volcán Alcedo, Galápagos," *J. Geophys. Res., Solid Earth*, vol. 112, no. B7, 2007, Art. no. B07407, doi: 10.1029/2006JB004763.
[14] A. Hooper, D. Bekaert, K. Spaans, and M. Arıkan, "Recent advances in SAR interferometry time series analysis for measuring crustal deformation," *Tectonophysics*, vols. 514–517, pp. 1–13, Jan. 2012, doi: 10.1016/j.tecto.2011.10.013.
[15] Q. Sun, Z.-W. Li, J.-J. Zhu, X.-L. Ding, J. Hu, and B. Xu, "Improved Goldstein filter for InSAR noise reduction based on local SNR," *J. Central South Univ.*, vol. 20, no. 7, p. 1896, 2013, doi: 10.1007/s11771-013-1688-3.
[16] H. Fattahi and F. Amelung, "InSAR bias and uncertainty due to the systematic and stochastic tropospheric delay," *J. Geophys. Res. Solid Earth*, vol. 120, no. 12, pp. 8758–8773, 2015, doi: 10.1002/2015JB012419.
[17] D. A. Schmidt and R. Bürgmann, "Time-dependent land uplift and subsidence in the Santa Clara valley, California, from a large interferometric synthetic aperture radar data set," *J. Geophys. Res.–Solid Earth*, vol. 108, no. B9, p. 2416, 2003, doi: 10.1029/2002JB002267.
[18] C.-W. Lee, Z. Lu, and H.-S. Jung, "Simulation of time-series surface deformation to validate a multi-interferogram InSAR processing technique," *Int. J. Remote Sens.*, vol. 33, no. 22, pp. 7075–7087, 2012, doi: 10.1080/01431161.2012.700137.
[19] A. L. B. Candeias, J. C. Mura, L. V. Dutra, and J. R. Moreira, "Interferogram phase noise reduction using morphological and modified median filters," in *Proc. IGARSS*, vol. 1, Jul. 1995, pp. 166–168, doi: 10.1109/IGARSS.1995.519679.
[20] R. Lanari *et al.*, "Generation of digital elevation models by using SIR-C/X-SAR multifrequency two-pass interferometry: The Etna case study," *IEEE Trans. Geosci. Remote Sens.*, vol. 34, no. 5, pp. 1097–1114, Sep. 1996, doi: 10.1109/36.536526.
[21] N. E. Huang *et al.*, "The empirical mode decomposition and the Hilbert spectrum for nonlinear and non-stationary time series analysis," *Proc. Roy. Soc. London Ser. A, Math., Phys. Eng. Sci.*, vol. 454, no. 1971, pp. 903–995, Mar. 1998, doi: 10.1098/rspa.1998.0193.
[22] G. Liu *et al.*, "Filtering SAR interferometric phase noise using a split-window model," *Remote Sens. Lett.*, vol. 7, no. 8, pp. 800–809, 2016, doi: 10.1080/2150704X.2016.1187316.
[23] T. R. Lauknes, H. A. Zebker, and Y. Larsen, "InSAR deformation time series using an L_1-norm small-baseline approach," *IEEE Trans. Geosci. Remote Sens.*, vol. 49, no. 1, pp. 536–546, Jan. 2011, doi: 10.1109/TGRS.2010.2051951.
[24] J. Biggs, T. Wright, Z. Lu, and B. Parsons, "Multi-interferogram method for measuring interseismic deformation: Denali Fault, Alaska," *Geophys. J. Int.*, vol. 170, no. 3, pp. 1165–1179, 2007, doi: 10.1111/j.1365-246X.2007.03415.x.
[25] Z. Y. Suo, Z. F. Li, and Z. Bao, "A new strategy to estimate local fringe frequencies for InSAR phase noise reduction," *IEEE Geosci. Remote Sens. Lett.*, vol. 7, no. 4, pp. 771–775, Oct. 2010, doi: 10.1109/LGRS.2010.2047935.
[26] C.-A. Deledalle, L. Denis, F. Tupin, A. Reigber, and M. Jäger, "NL-SAR: A unified nonlocal framework for resolution-preserving (Pol)(In)SAR denoising," *IEEE Trans. Geosci. Remote Sens.*, vol. 53, no. 4, pp. 2021–2038, Apr. 2015, doi: 10.1109/TGRS.2014.2352555.
[27] C.-A. Deledalle, L. Denis, and F. Tupin, "Iterative weighted maximum likelihood denoising with probabilistic patch-based weights," *IEEE Trans. Image Process.*, vol. 18, no. 12, pp. 2661–2672, Dec. 2009, doi: 10.1109/TIP.2009.2029593.
[28] F. Takens, *Lecture Notes in Math*, vol. 898. Berlin, Germany: Springer-Verlag: 1981.
[29] F. Hamilton, T. Berry, and T. Sauer, "Ensemble Kalman filtering without a model," *Phys. Rev. X*, vol. 6, no. 1, 2016, Art. no. 011021, doi: 10.1103/PhysRevX.6.011021.
[30] M. Khaki, F. Hamilton, E. Forootan, I. Hoteit, J. Awange, and M. Kuhn, "Nonparametric data assimilation scheme for land hydrological applications," *Water Resour. Res.*, vol. 54, no. 7, pp. 4946–4964, Jul. 2018, doi: 10.1029/2018WR022854.
[31] M. Khaki, I. Hoteit, M. Kuhn, E. Forootan, and J. Awange, "Assessing data assimilation frameworks for using multi-mission satellite products in a hydrological context," *Sci. Total Environ.*, vol. 647, pp. 1031–1043, Jan. 2019, doi: 10.1016/j.scitotenv.2018.08.032.
[32] J. J. Martinez-Espla, T. Martinez-Marin, and J. M. Lopez-Sanchez, "A particle filter approach for InSAR phase filtering and unwrapping," *IEEE Trans. Geosci. Remote Sens.*, vol. 47, no. 4, pp. 1197–1211, Apr. 2009, doi: 10.1109/TGRS.2008.2008095.
[33] Y. Gao, S. Zhang, T. Li, Q. Chen, S. Li, and P. Meng, "Adaptive unscented Kalman filter phase unwrapping method and its application on Gaofen-3 interferometric SAR data," *Sensors*, vol. 18, no. 6, p. 1793, 2018, doi: 10.3390/s18061793.
[34] K. R. Koch, *Introduction to Bayesian Statistics*, 2nd ed. Berlin, Germany: Springer, 2007.
[35] M. Khaki *et al.*, "Assessing sequential data assimilation techniques for integrating GRACE data into a hydrological model," *Adv. Water Resour.*, vol. 107, pp. 301–316, Sep. 2017, doi: 10.1016/j.advwatres.2017.07.001.
[36] M. Khaki, B. Ait-El-Fquih, I. Hoteit, E. Hoteit, J. Awange, and M. Kuhn, "Unsupervised ensemble Kalman filtering with an uncertain constraint for land hydrological data assimilation," *J. Hydrol.*, vol. 564, pp. 175–190, Sep. 2018, doi: 10.1016/j.jhydrol.2018.06.080.
[37] F. Hamilton, T. Berry, and T. Sauer, "Kalman-Takens filtering in the presence of dynamical noise," *Eur. Phys. J. Special Topics*, vol. 226, no. 15, pp. 3239–3250, Dec. 2017, doi: 10.1140/epjst/e2016-60363-2.
[38] T. Berry and T. Sauer, "Adaptive ensemble Kalman filtering of non-linear systems," *Tellus A, Dyn. Meteorol. Oceanogr.*, vol. 65, no. 1, p. 20331, 2013, doi: 10.3402/tellusa.v65i0.20331.
[39] M. S. Arulampalam, S. Maskell, N. Gordon, and T. Clapp, "A tutorial on particle filters for online nonlinear/non-Gaussian Bayesian tracking," *IEEE Trans. Signal Process.*, vol. 50, no. 2, pp. 174–188, 2002, doi: 10.1109/78.978374.
[40] A. Doucet and A. M. Johanse, "A tutorial on particle filtering and smoothing: Fifteen years later," in *The Oxford Handbook of Nonlinear Filtering*, D. Crisan and B. Rozovskii, Eds. New York, NY, USA: Oxford Univ. Press, 2008, pp. 656–704.
[41] E. A. Wan and R. van der Merwe, *The Unscented Kalman Filter*. Hoboken, NJ, USA: Wiley, 2001.
[42] M. Klaas, M. Briers, N. de Freitas, A. Doucet, S. Maskell, and D. Lang, "Fast particle smoothing: If I had a million particles," in *Proc. 23rd Int. Conf. Mach. Learn. (ICML)*, Pittsburgh, PA, USA, 2006, pp. 481–488, doi: 10.1145/1143844.1143905.
[43] A. Douc and O. Cappe, "Comparison of resampling schemes for particle filtering," in *Proc. 4th Int. Symp. Image Signal Process. Anal. (ISPA)*, Zagreb, Croatia, 2005, pp. 64–69, doi: 10.1109/ISPA.2005.195385.
[44] H. Breit, T. Fritz, U. Balss, M. Lachaise, A. Niedermeier, and M. Vonavka, "TerraSAR-X SAR processing and products," *IEEE Trans. Geosci. Remote Sens.*, vol. 48, no. 2, pp. 727–740, Feb. 2010, doi: 10.1109/TGRS.2009.2035497.
[45] B. M. Kampes and S. Usai, "Doris: The Delft object-oriented radar interferometric software," Delft Inst. Earth Observation Space Syst., Delft Univ. Technol., Delft, The Netherlands, Tech. Rep. v4.02, 1999.
[46] A. Doucet, N. Freitas, K. Murphy, and S. Russell, "Rao blackwellised particle filtering for dynamic Bayesian networks," in *Uncertainty in Artificial Intelligence*, C. Boutilier and M. Godszmidt, Eds. San Mateo, CA, USA: Morgan Kaufmann, 2000, pp. 176–183.
[47] T. Fuhrmann and M. C. Garthwaite, "Resolving three-dimensional surface motion with InSAR: Constraints from multi-geometry data fusion," *Remote Sens.*, vol. 11, no. 3, p. 241, 2019.

Mehdi Khaki received the Bachelor of Civil Engineering degree in surveying and the M.Sc. degree in geodesy from the University of Tehran, Tehran, Iran, in 2011 and 2014, respectively, and the Ph.D. degree from Curtin University, Perth, WA, Australia, in 2018, working on satellite data assimilation.

He is currently a Lecturer with the School of Engineering, University of Newcastle, Callaghan, NSW, Australia. His research interests include the application of geodetic and remote sensing techniques and their integration with land surface models to improve their simulations. His research also involves developing and implementing numerical and statistical methods in Earth science studies.

Mick S. Filmer received the Bachelor of Geoinformatics and Surveying degree (Hons.) from the University of South Australia, Adelaide, SA, Australia, in 2004, and the Ph.D. degree from Curtin University, Perth, WA, Australia, in 2011.

He was a Post-Doctoral Research Associate with Curtin University from 2011 to 2014, where he was involved in the Australian Research Council-funded Linkage Project monitoring land deformation in the Perth Basin using InSAR, GPS, and leveling. Since September 2014, he has been a Lecturer with Curtin University, continuing his research in the Perth Basin, focusing on using TerraSAR-X data to estimate land subsidence/uplift. His research interests include the application of InSAR and GPS to determine vertical land motion, time series estimation, coastal oceanography, and vertical datum unification.

Will E. Featherstone received the B.Sc. degree (Hons.) in geophysics and planetary physics from Newcastle University, Newcastle upon Tyne, U.K., in 1988, and the D.Phil. degree in geodesy from Oxford University, Oxford, U.K., in 1992.

He is currently a Professor of geodesy with Curtin University, Perth, WA, Australia, and a Visiting Professor with IIT Kanpur, Kanpur, India. His research interests range from gravity field and height determination and modeling, using geodesy to study the sea-level record and using satellite radar to monitor land subsidence, through to the use of gravity and topography to locate new craters on the moon.

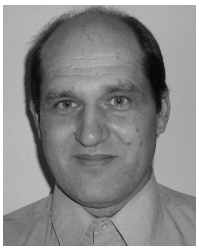

Michael Kuhn received the Diploma degree in surveying and the Ph.D. degree in physical geodesy from the University of Karlsruhe [now Karlsruhe Institute of Technology (KIT)], Karlsruhe, Germany, in 1994 and 1999, respectively.

He was a Research Associate with the German Geodetic Research Institute (DGFI), Munich, Germany, from 1999 to 2001, where he was involved in the monitoring of anomalous sea-level variations in the North Atlantic. In 2001, he joined the Discipline of Spatial Sciences, Curtin University, Perth, WA, Australia. He held a Post-Doctoral Fellowship at the Australian Research Council from 2003 to 2007, a Curtin University Research and Teaching Fellowship from 2007 to 2012, and currently holds the position of an Associate Professor. His research interests include physical geodesy, oceanography, and environmental sciences with a focus on global high-resolution gravity forward modeling, synthetic Earth gravity modeling, sea-level variability, and space geodetic monitoring of environmental processes.

Dr. Kuhn is a fellow of the International Association of Geodesy (IAG) and chaired two IAG study groups on synthetic gravity modeling and gravity forward modeling from 2003 to 2011.

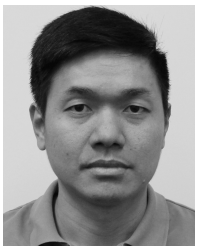

Luyen K. Bui received the M.S. degree in geodesy from the University of Mining and Geology, Hanoi, Vietnam, in 2010. He is currently pursuing the Ph.D. degree in InSAR data processing with the Geodesy Laboratory, School of Earth and Planetary Sciences, Curtin University, Perth, WA, Australia.

His research interests include InSAR signal processing and applications, assessing noise in InSAR data, and optimal design of InSAR SBAS networks.

Amy L. Parker received the Bachelor of Geophysics degree (Hons.) from the University of Liverpool, Liverpool, U.K., in 2011, and the Ph.D. degree in geology from the University of Bristol, Bristol, U.K., in 2015.

Since 2015, she has been undertaking Post-Doctoral Research at Curtin University, Perth, WA, Australia, where she currently holds the Australian Research Council Discovery Early Career Researcher Fellowship. Her research involves the application of InSAR to monitor natural hazards, including volcanos, earthquakes, and the effects of groundwater extraction.